Renewable Energy 263 (2026) 125497

Contents lists available at ScienceDirect

Renewable Energy

journal homepage: www.elsevier.com/locate/renene

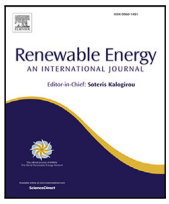

Coastal response to wave energy converter arrays: A semi-analytical model for control of nearshore currents and beach morphology

Lidong Cui [a,*], Nataliia Y. Sergiienko [b], Nadav Cohen [c], Justin S. Leontini [a], Benjamin S. Cazzolato [b], Francois Flocard [c], Richard Manasseh [a]

[a] Department of Mechanical and Product Design Engineering, Swinburne University of Technology, Hawthorn, 3122, Victoria, Australia
[b] School of Electrical and Mechanical Engineering, College of Engineering and Information Technology, Adelaide University, Adelaide, 5005, South Australia, Australia
[c] Water Research Laboratory, School of Civil and Environmental Engineering, UNSW Sydney, Manly Vale, 2093, New South Wales, Australia

ARTICLE INFO

Keywords:
Wave energy converters
Longshore sediment transport
Longshore current
Rip current
Nearshore circulation
Beach erosion
Coastal management

ABSTRACT

A semi-analytical method much faster than typical computational and experimental methods is developed to quantify how wave energy converter arrays ("wave farms") affect nearshore currents and beach erosion through modifying ocean waves. The method provides a semi-analytical initial design tool for evaluating coastal impacts of wave farms. The method integrates an existing semi-analytical wave farm model with a nearshore current model; the latter is a rip current model, here it is modified to tackle the wave field produced by wave energy converter arrays. The method is validated against a classic example and compared to results from numerical simulations and wave basin experiments, for an array of 16 oscillating water column devices. The method is then implemented optimise the 16-device array to increase its ability to protect the beach. It is found that the arrays most effective for beach protection also perform well in energy generation. This suggests that prioritising beach protection does not necessarily compromise energy generation performance.

1. Introduction

Wave-energy converters (WECs) extract renewable energy from ocean waves, mostly for conversion to electricity. While many classes of WECs have been successfully trialled, their levelised cost of electricity (LCOE) is at present too high to compete directly with the best-established forms of renewable energy; a recent summary of WEC LCOEs analyses [1] suggests a 2025 value over €200 per megawatt-hour, over six times the cost of onshore wind [2]. However, reviews have increasingly emphasised that WECs also offer unique coastal-protection opportunities [3–5], which may completely alter their economic viability as renewable-energy generators.

With demonstrations [*e.g.* 6] that coastal flooding will become more frequent, the demand for coastal protection is increasing. Conventional coastal protection methods such as submerged breakwaters [7] and surface-piercing breakwaters [8] are usually fixed and cannot actively adapt to an evolving environment. New, adaptive coastal protection technologies are being developed; these include *dual-purpose WECs* aimed at both influencing the coastal environment and simultaneously generating renewable energy. Designed as resonators to interact with incoming waves, these dual-purpose WECs offer a high degree of tunability [9,10] and they are proposed to be deployed in the form of arrays (farms) to exploit favourable inter-device hydrodynamic interactions [11]. By changing device tuning and array layout, it is possible for an array to adapt to a changing climate. Examples of laboratory-scale offshore dual-purpose WEC arrays [12,13] are shown in Fig. 1, together with a beach it intends to protect. Although these particular array layouts will not be discussed in this paper (as they were not designed to measure nearshore currents), elements from these experiments, such as equipment, basin set-up, and beach geometry, will be revisited in the later sections of this paper.

Some general considerations are needed when developing dual-purpose offshore WEC arrays. These include (1) describing the behaviour of an individual device; (2) characterising inter-device hydrodynamic interactions, and (3) evaluating the WEC array's coastal impacts. Computational [*e.g.* 14,15] and experimental approaches [*e.g.* 12, 16] yield relatively more accurate results but they are limited by the cost, thus they can be impractical for comparing many (*e.g.* $O(10^4)$) different WEC array layouts required for design optimisation purpose. Semi-analytical or analytical methods are faster and are hence able to compare a large number of designs. For example, in [17], a semi-analytical method is developed to seek a WEC array layout that

* Corresponding author.
E-mail address: LCui@swin.edu.au (L. Cui).

https://doi.org/10.1016/j.renene.2026.125497
Received 13 October 2025; Received in revised form 24 January 2026; Accepted 24 February 2026
Available online 26 February 2026

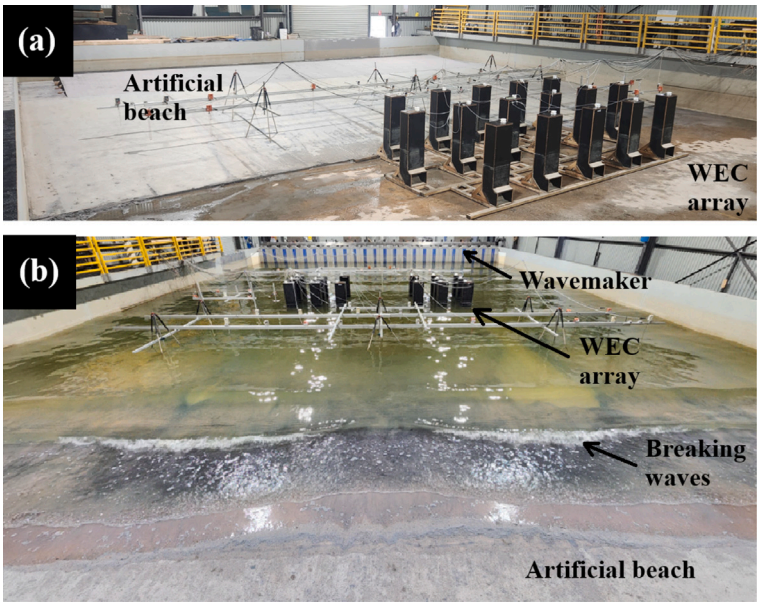

Fig. 1. (a) a dual-purpose offshore wave energy converter (WEC) array (black-coloured) tested in the 28 × 16 m wave basin of the Water Research Laboratory (WRL) of the University of New South Wales (Australia) with an initially 2D artificial beach (as shown). The WECs are L-shaped oscillating water column (OWC) devices with effective length of 565 mm and rectangular cross-section measuring 0.2 × 0.3 m. They are each equipped with an orifice of 35 mm diameter to represent power-take-off (PTO). More details can be found in the Supplementary Material. All 16 devices have the same specifications. The basin is shown empty but when filled with water, the offshore water depth is 0.586 m; (b) due to wave modification by the WEC array, the 2D beach is modified to 3D. The peak period of the incident wave (JONSWAP spectrum) is T_p = 1.6 s. Note that the array layout in panel (a) differs from (b); many different array layouts are tested in [12].

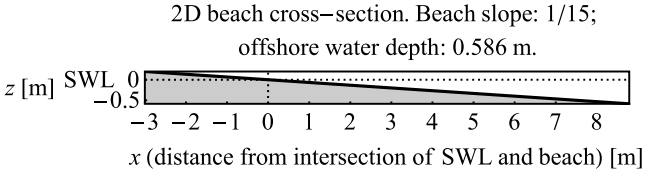

Fig. 2. Profile of the initially 2D laboratory beach used in Fig. 1. Drawn to scale. Grey-coloured region represents the beach; SWL is still water level. Waves incident from right to left.

reduces wave amplitude as much as possible, quantified by the size of a "wave shadow" in which the transmission coefficient is reduced. While existing semi-analytical methods focus on modifying waves, coastal protection is about more than attenuating waves, as revealed by the experiments in [12]. Wave-induced nearshore currents are also important, as two WEC arrays producing similar-sized wave shadows can lead to very different nearshore currents, and cause dissimilar beach erosion and accretion modes. In addition to erosion, nearshore currents can also affect beach-related sports and leisure activities [*e.g.* 18,19] which can impact a significant number of beach users: during 2011–2021, in Australia alone, 3.7 million beach users were trapped by rip currents [20]. Moreover, intertidal organisms and aquaculture can be affected by currents [21,22]. These necessitate a nearshore current model to supplement the wave model in [17].

In view of the above needs, this paper (i) develops a fast semi-analytical method to relate the wave shadow generated by a dual-purpose WEC array to nearshore currents, (ii) relates these currents to beach erosion, and (iii) finds the optimal WEC array layouts that create desirable nearshore currents. This paper approaches the task (i) by extending the method in a seminal paper [23] (which is limited to a wave shadow with relatively simple shape, see Appendix A) to arbitrary-shaped wave shadows such as those generated by some WEC arrays. Task (ii) is resolved by a semi-empirical formula. Task (iii) is accomplished by a straightforward optimisation routine. On an entry-level personal laptop computer, all three tasks can be performed within 20 min for a laboratory-scale 16-device WEC array for simple wave conditions and canonical bathymetries.

This paper is structured as follows. Section 2 explains the phenomenon of nearshore currents and extends the semi-analytical method for nearshore currents proposed by [23] to generic cases (*i.e.* wave shadows with arbitrary shapes). Although such an extension does not require a new mathematical paradigm, it involves new algebraic details and to ensure the repeatability of results, many additional intermediate steps neglected in [23] are provided in full detail in the Supplementary Material. Section 3 validates the calculated nearshore currents against recent numerical and experimental results. Section 4 relates nearshore currents to beach modification by a formula proposed by [24], and discusses how the desired beach modifications can be obtained by optimising the WEC array layout, leading to two new WEC array designs under two different design goals. Finally, Section 5 summarises the key findings and limitations of the paper.

2. Nearshore currents: phenomenology and modelling

It should be mentioned at the beginning that the nearshore current model does not include ambient ocean currents; instead, it focuses on wave-induced currents only.

Mathematical models for nearshore currents are of limited applicability to natural beaches [25], but it is expected that they can be of value in terms of order-of-magnitude estimations and physical explanations. A classic model is due to [23]; but before diving into details of any model, this section discusses first the phenomenon to be modelled.

It is convenient and conventional to parse the velocity of the nearshore currents into cross-shore (perpendicular to the coastline, x) and longshore (parallel to the coastline, y) components. The velocity can also be in the z-direction (perpendicular to the still water surface, see [*e.g.* 26]), but as an initial study, one can assume that the flow structures are predominantly horizontal [*e.g.* 27] so that the z-velocity

Fig. 3. Cross-shore currents on Bells Beach, Victoria, Australia. (a) "up-rush", *i.e.* bore travelling up the beach after wave breaking; (b) "backwash" ("swash rip currents"), featuring currents flowing offshore (*cf.* Fig. 7 of [31]). Photographs taken by L.C. on 5 April 2015, at 1207 and 1210 local times, respectively. Location: 38° 22′ 3.7″ S, 144° 17′ 5.9″ E.

is neglected. Cross-shore currents are explained first; longshore currents are explained subsequently.

2.1. Phenomenology and physical mechanisms

2.1.1. Cross-shore currents due to set-up and set-down

While perfect cross-shore currents are not expected to exist on natural beaches, on some beaches, the currents can be predominantly cross-shore. Fig. 3 shows such a case: breaking wave induced cross-shore currents dominant at Bells Beach (Victoria, Australia) despite local longshore currents created by beach cusps [*e.g.* 28,29].

From a modelling point of view, cross-shore currents are water flows from the high mean water line (MWL) region (*i.e.* set-up region) to the low MWL region (*i.e.* set-down region) due to gravity. The low MWL region corresponds to the shoaling zone (*i.e.* before the waves break on the beach): as surface waves travel up the beach, water depth becomes shallower, wave height increases, and radiation stress rises, which lowers the MWL [*e.g.* 23,30], causing set-down. The high MWL region corresponds to the surf zone where wave height is reduced due to breaking, and the sign of the radiation stress is reversed; this raises the MWL, causing set-up.

To illustrate set-down and set-up in a controlled laboratory environment, consider the experiment set-up from [12], where a small, idealistic, initially-2D model sandy beach is used, see Fig. 1. Fig. 2 depicts the beach diagrammatically. This 2D beach's slope is 1/15 and it extends to an offshore water depth of 0.586 m.

At this stage, consider the case without WEC array, to illustrate nearshore currents. Monochromatic surface waves are generated with offshore wave height $H_0 = 0.05$ m and wave period $T = 1.6$ s, normally incident onto the beach. When the wave encounters the beach, it undergoes shoaling and eventually breaks (*cf.* Fig. 1b). The associated set-down and set-up of MWL are quantified using the method in the Supplementary Material, and are plotted in Fig. 4. Fig. 4 contains the following key information:

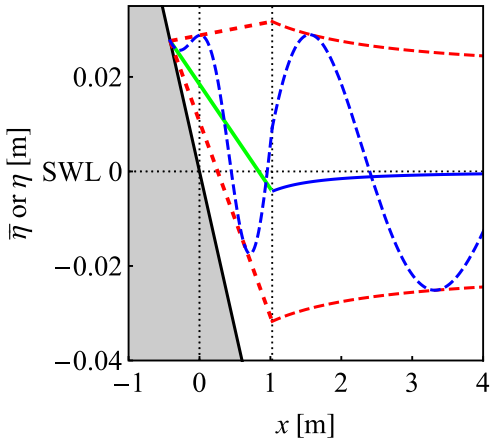

Fig. 4. Semi-analytical plots of wave elevation and mean water level (MWL) for the 2D beach shown in Fig. 2. Monochromatic waves incident from the right side of the figure; offshore wave height is 0.05 m (amplitude: 0.025 m); period is 1.6 s. - - - - indicates instantaneous surface wave elevation; wave height envelope is indicated by - - - -; MWL is represented by —— in the shoaling zone (before wave-breaking); —— indicates MWL in the surf zone (after wave-breaking). The wave breaking location is marked by a vertical dotted black line at $x \approx 1.02$ m.

(1) the original offshore wave height H_0 slightly increases as the wave propagates towards the coastline, due to conservation of mass in the shoaling process;
(2) set-down: the MWL decreases as (1) takes place;
(3) set-up: the MWL increases as the wave height quickly decreases once the wave breaks and becomes a bore that continues to proceed up the beach, creating the surf zone;
(4) a cross-shore current will be created, flowing offshore (the current is not shown in Fig. 4).

Also observable in Fig. 4 is *run-up* (red dashed lines in the surf zone: broken wave height). It is the sum of setup and half the swash height (oscillatory motion of broken waves) [32].

2.1.2. Longshore currents due to inhomogeneous set-up

Although pure cross-shore currents may be produced on a laboratory 2D beach with 2D long-crested normally-incident waves, the Nature always provides 3D features that lead to spanwise-inhomogeneous set-up and set-down, which leads to spanwise variations in MWL, which leads to longshore currents. One mechanism to cause such spanwise variations is visible in Fig. 3(b): beach cusps change the local slope of the beach and increase the local MWL. Other mechanisms include oblique waves [33], wave–current interaction [34], bathymetric irregularities beyond the surf zone [35], intersecting ocean wave trains [36], and rip channels [37].

In the context of this paper, the spanwise variations will be caused by the spanwise inhomogeneities in offshore wave height H_0 generated by presence of WEC arrays. Specifically, an array creates a "wave shadow" [17], in which H_0 is reduced; a beach section corresponding to lower H_0 receives lower set-up (lower MWL), and *vice versa*. Water thus flows from the high MWL to the low MWL region, generating longshore currents. The details of such spanwise variations in H_0 depend on the WEC array layout, providing an opportunity of finding optimal spanwise variations that maximises beach protection.

2.2. Modelling

2.2.1. Cross-shore currents: revisiting a classic theory

We explain very briefly how in Fig. 4 the quantities, which lead to cross-shore currents, can be calculated by the classic theory in [23].

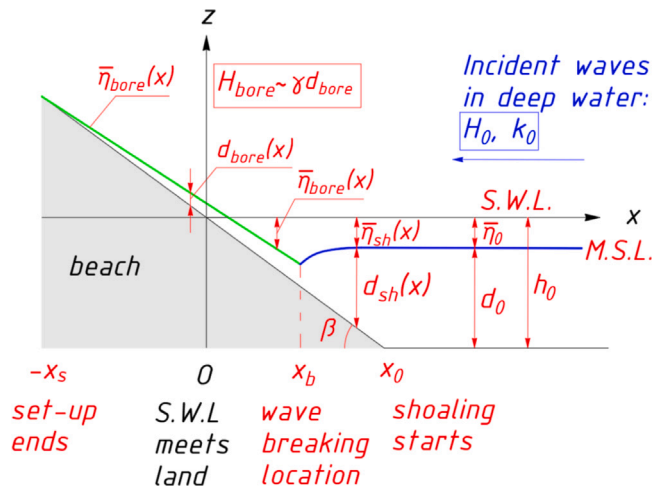

Fig. 5. A schematic of nearshore hydrodynamics near a 2D beach (*cf.* Fig. 4). On the x-axis, x_b is the wave breaking location, x_s is the location of the maximum set-up, x_0 marks the end of the beach slope. In the offshore water ($x > x_0$), set-down of the MWL (mean water level) is measured by $\bar{\eta}_0$. In the shoaling zone ($x_0 > x > x_b$), set-down is $\bar{\eta}_{sh}(x)$; in the surf zone ($x_s < x < x_b$), set-down is $\bar{\eta}_{bore}(x)$; at the wave breaking point ($x = x_b$), set-down is $\bar{\eta}_{br}$. Moreover, β is the beach's angle satisfying $\beta = \tan^{-1}\tilde{m}$ where $\tilde{m}$ is the beach slope. Offshore water depth is d_0; in the shoaling zone, water depth is $d_{sh}(x)$; in the surf zone, $d_{bore}(x)$; at the wave breaking point, d_{br}. H_0, k_0 are offshore incident wave height and wave number. The beach is uniform on the y-direction (not shown). Interested readers can also refer to Fig. 2 of [38] for a broader perspective of nearshore processes.

Here we merely explain the symbol system and present the modelling framework, while leaving the algebraic details in the Supplementary Material which contains step-by-step derivations of some results in [23].

To facilitate analysis, Fig. 4 is re-drawn to Fig. 5, where waves quantities are removed (only mean water levels are shown), and scales are distorted for clarity. In Fig. 5, the x-axis is placed at the still water line SWL; the z-axis is placed at the intersection of the SWL and the beach. The beach is described by its slope $\tilde{m}$. The offshore (where the bottom is flat) set-down $\bar{\eta}_0$ as a function of H_0, k_0, h_0 (the offshore wave height, wavenumber, and still water depth) is first determined by a well-known formula [30,39]. With $\bar{\eta}_0$ determined, the water depth measured against MWL, denoted by d_0, is determined by $h_0 - \bar{\eta}_0$.

Next, the set-down in the shoaling zone (from the start of the beach x_0 to the wave breaking point x_b), denoted by $\bar{\eta}_{sh}(x)$, is determined [23, 40] as a function of $H_0, k_0, k(x), h(x)$ where $k(x)$ and $h(x)$ are local wavenumber and still water depth; they change with x due to the beach slope. With $\bar{\eta}_{sh}(x)$ determined, the water depth measured against MWL before wave breaking, denoted by d_{sh} (see Fig. 5), is determined by $\bar{\eta}_{sh}(x) + h(x)$. The aforementioned wave breaking location x_b and the water depth at the wave breaking location, h_b, are determined by empirical formulas (the wave height in the shoaling zone H_{sh} can also be calculated by the method in [40] and it appeared in Fig. 4 but not in Fig. 5, as it is less relevant to the ensuing sections of this paper).

Onto the surf zone ($x < x_b$), the set-up $\bar{\eta}_{bore}$ is calculated as a function of $\gamma, \tilde{m}, x$ where γ is an empirical constant ranging from 0.90 to 1.28 [40]. In this paper, 1.15 is used. A matching condition ensures the continuity of $\bar{\eta}_{bore}$ and $\bar{\eta}_{sh}$ at x_b. The left-extreme of the surf zone is marked by a negative number x_s; it is the intersection location of $\bar{\eta}_{bore}$ and the beach. In the surf zone, the water depth measured against MWL is denoted by d_{bore} and the wave (bore) height H_{bore} is calculated by the following formula [23]:

$$H_{bore}(x) = \gamma\tilde{m}(1-K)(x - x_s). \tag{1}$$

where

$$K = \frac{1}{1 + \frac{8}{3\gamma^2}}. \tag{2}$$

Once H_{bore} is given by Eq. (1), the water depth d_{bore} (see Fig. 5) is given by:

$$d_{bore} = \frac{H_{bore}}{\gamma}. \tag{3}$$

Both Eqs. (1) and (3) are used later in calculating nearshore currents.

2.2.2. Baseline model of longshore currents and present extensions for wave farm applications

$H_{bore}(x)$ expressed by Eq. (1) is y-independent. When the y-independency is lost, longshore currents can be created which, when combined with cross-shore currents, creates nearshore circulations. In [23], it is assumed that $H_{bore}(x, y)$ has a sinusoidal variation in the y-direction specified by $1 + \epsilon\cos(\lambda y)$:

$$H_{bore}(x, y) = \gamma\tilde{m}(1-K)(x - x_s)\,[1 + \epsilon\cos(\lambda y)] \tag{4}$$

where ϵ is a small parameter and λ is a wavenumber in the y direction. In this paper, to deal with WEC-generated wave fields, we generalise the above sinusoidal function to an arbitrary function $f(y)$ with the expectation that it can be approximated by a Fourier series with a finite number of sinusoidal modes:

$$H_{bore}(x, y) = \gamma\tilde{m}(1-K)(x - x_s)f(y); \tag{5}$$

$$f(y) = \mathfrak{a}_0 + \sum_{n=1}^{N} \mathfrak{a}_n \cos(n\lambda y + \theta_n), \tag{6}$$

where $\mathfrak{a}_0$ is a real constant, usually closer to 1 than to 0 for typical sparse WEC arrays, $\mathfrak{a}_n$ are real constants usually much smaller than 1, θ_n are phase angles, n and N are integers. In the case of WEC modelling, $f(y)$ is the incident wave's transmission coefficient function $f(x, y)$ evaluated at a particular offshore x location of interest. It can be given by a wave–WEC interaction model [17]. Here the transmission coefficient is defined as the amplitude of waves normalised by the incident wave amplitude. When it equals 1, the wave height is not changed; when it equals 0, all waves are eliminated. The functional form of $f(y)$ can be rather complicated, such that sometimes approximately ten modes are necessary in Eq. (6). Now define a real-valued quantity B_n that contains $\mathfrak{a}_n$ (in Eq. (6)):

$$B_n \equiv -\frac{1}{4}g\gamma^2\tilde{m}(1-K)n\lambda\mathfrak{a}_n \text{ (where } g \approx 9.81 \text{ m/s}^2), \tag{7}$$

and define a stream function ψ in the surf zone. Using the method in [23] but extending the method to accommodate the arbitrary form of $f(y)$ presented by Eq. (6), the following governing equation is obtained (see Supplementary Material for a derivation):

$$\frac{1}{d_{bore}(x)^2}\nabla^2\psi - \frac{2}{d_{bore}(x)^3}\tilde{m}(1-K)\frac{\partial\psi}{\partial x} = \sum_{n=1}^{N}\frac{B_n}{c}\sin(n\lambda y + \theta_n) \tag{8}$$

where c is an empirical bottom friction coefficient. When $f(y) = 1 + \epsilon\cos(\lambda y)$, the RHS of Eq. (8) recovers Eq. (34) of [23]. The boundary condition for Eq. (8) reads [23]:

$$\psi(x_s, y) = 0, \tag{9}$$

which physically indicates that there is no flow past x_s (*cf.* Fig. 5).

The system consisting Eq. (8), (9) can be solved using the approach in [23] although the algebraic details are different due to a more

complicated $f(y)$. The following solution is appropriate:

$$\begin{aligned}\psi &= \sum_{n=1}^{N}\psi_n \\ &= \sum_{n=1}^{N}\sin(n\lambda y+\theta_n)\left\{P_n\left[n\lambda(x-x_s)\cosh n\lambda(x-x_s)-\sinh n\lambda(x-x_s)\right]+\right. \\ &\quad \frac{B_n\widetilde{m}^2(1-K^2)}{c(n\lambda)^4}\left[2-(n\lambda)^2(x-x_s)^2+2n\lambda(x-x_s)\sinh n\lambda(x-x_s)\right. \\ &\quad \left.\left.-2\cosh n\lambda(x-x_s)\right]\right\},\end{aligned} \tag{10}$$

where P_n are unknown coefficients. Note that when $N=1,\theta_1=0$, the above becomes Eq. (35) of [23] if $B_1\equiv B, P_1\equiv P$.

Now the stream function in the shoaling zone is discussed. Denote the solution in the shoaling zone by ψ^{sh}. The governing equation for ψ^{sh} is Eq. (8) without forcing terms and with $d_{\mathrm{bore}}(x)$ replaced by $d_{\mathrm{sh}}(x)$:

$$\frac{1}{d_{\mathrm{sh}}(x)^2}\nabla^2\psi^{\mathrm{sh}}-\frac{2}{d_{\mathrm{sh}}(x)^3}\widetilde{m}(1-K)\frac{\partial\psi^{\mathrm{sh}}}{\partial x}=0. \tag{11}$$

The solution below holds:

$$\begin{aligned}\psi^{\mathrm{sh}} &= \sum_{n=1}^{N}\psi_n^{\mathrm{sh}} \\ &= \sum_{n=1}^{N}Q_n\left[n\lambda(x-x_s)+1\right]\mathrm{e}^{-n\lambda(x-x_s)}\sin(n\lambda y+\theta_n),\end{aligned} \tag{12}$$

where Q_n are unknown coefficients. When $N=1,\theta_1=0,Q_1\equiv Q$, Eq. (12) becomes Eq. (36) of [23]. The unknown coefficients P_n, Q_n in Eqs. (10), (12) are determined by the following matching conditions at wave breaking location x_b which states that streamfunctions in the shoaling and surf zones should match:

$$\begin{cases}\psi_n=\psi_n^{\mathrm{sh}}\big|_{x=x_b}, \\ \dfrac{\partial\psi_n}{\partial x}=\dfrac{\partial\psi_n^{\mathrm{sh}}}{\partial x}\Big|_{x=x_b}.\end{cases} \tag{13}$$

Now that ψ_n and ψ_n^{sh} are determined, ψ and ψ^{sh} can be calculated. The surf zone current velocities u and v, and the shoaling zone velocities u^{sh} and v^{sh} are specified by [23]:

$$\begin{aligned}u=-\frac{1}{d_{\mathrm{bore}}(x)}\frac{\partial\psi}{\partial y},\quad v=\frac{1}{d_{\mathrm{bore}}(x)}\frac{\partial\psi}{\partial x}; \\ u_{\mathrm{sh}}=-\frac{1}{d_{\mathrm{bore}}(x)}\frac{\partial\psi_{\mathrm{sh}}}{\partial y},\quad v_{\mathrm{sh}}=\frac{1}{d_{\mathrm{bore}}(x)}\frac{\partial\psi_{\mathrm{sh}}}{\partial x},\end{aligned} \tag{14}$$

yielding

$$\begin{cases}u=-\dfrac{\partial\psi}{\partial y}\dfrac{1}{d_{\mathrm{bore}}(x)}=-\dfrac{\partial\psi}{\partial y}\dfrac{1}{\widetilde{m}(1-K)(x-x_s)}; \\ v=\dfrac{\partial\psi}{\partial x}\dfrac{1}{d_{\mathrm{bore}}(x)}=\dfrac{\partial\psi}{\partial x}\dfrac{1}{\widetilde{m}(1-K)(x-x_s)}; \\ u^{\mathrm{sh}}=-\dfrac{\partial\psi^{\mathrm{sh}}}{\partial y}\dfrac{1}{d_{\mathrm{sh}}(x)}=-\dfrac{\partial\psi^{\mathrm{sh}}}{\partial y}\dfrac{1}{h-\frac{1}{16}H_0^2k_0\frac{1}{\tanh^2(kh)\left[\sinh(kh)\cosh(kh)+kh\right]}}; \\ v^{\mathrm{sh}}=\dfrac{\partial\psi^{\mathrm{sh}}}{\partial x}\dfrac{1}{d_{\mathrm{sh}}(x)}=\dfrac{\partial\psi^{\mathrm{sh}}}{\partial x}\dfrac{1}{h-\frac{1}{16}H_0^2k_0\frac{1}{\tanh^2(kh)\left[\sinh(kh)\cosh(kh)+kh\right]}}.\end{cases} \tag{15}$$

As a summary, we note that it is clear that the details of $f(y)$ are crucial in determining nearshore currents, because the key outcome, the streamfunction Eq. (10), contains B_n which, according to Eq. (7), contains $\mathfrak{a}_n$ which, according to Eq. (6), are coefficients in $f(y)$.

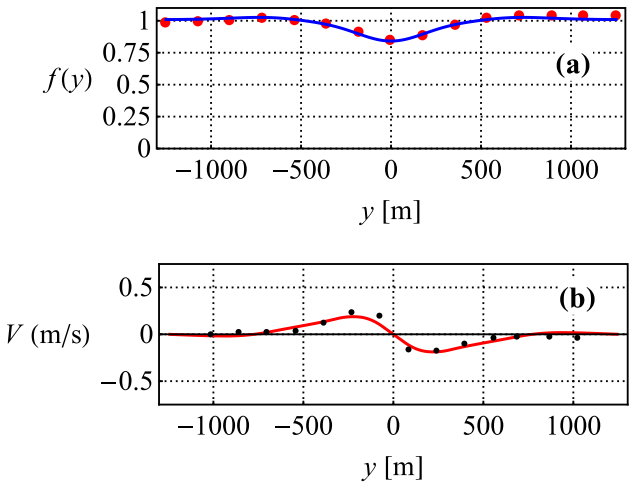

Fig. 6. Reproducing parts of Fig. 3 of [14] by the method in this paper. Panel (a) shows the function $f(y)$ (*cf.* Eq. (6)), obtained from the black curve in Fig. 3(d) of [14], with appropriate smoothing and normalisation. Red dots are data points extracted from Fig. 3(d) of [14] while the blue curve is the Fourier series fit. Panel (b) shows the resulting averaged longshore current velocity V. Red curve: present calculation; black dots: data extracted from Fig. 3 (j) of [14].

3. Comparing modelled currents with existing results

Validation/comparison is performed in increasing order of realism: (i) recovery of a classic analytical result, (ii) comparison with phase-resolving numerical simulations, and (iii) qualitative comparison with laboratory experiments.

3.1. Baseline validation: comparing modelled currents with results in [23]

Using the original, sinusoidal $f(y)$ in [23] (see Eq. (4)) and calculate nearshore currents, the results are presented in Appendix A, which shows that the present method can recover results in [23] almost exactly, as it should be, hence providing a basic validation of the algebraic details of the current model which is an extension of [23].

3.2. Comparing modelled currents with a numerical example

Through a phase-resolving numerical wave model, [14] considers full-scale straight beaches affected by WEC farms. The scope of [14] overlaps with the present paper; hence it is of interest to assess whether the semi-analytical method of the present paper can recover their results. Their 2500-metre-wide straight beach has a slope of $\widetilde{m}=1/50$, extending to an offshore water depth of 20 m. The paper uses as the base wave condition the JONSWAP spectrum with significant wave height H_s of 2 m, a peak period T_p of 10 s, and directional spreading $\sigma_\theta = 10°$. Wave farms are located offshore and produce a "wave shadow" so that breaking wave heights along the beach are modified, producing longshore currents.

In principle, one cannot expect the results in [14] to be replicated accurately by the present work, because we use monochromatic and normally-incident incident waves with $\sigma_\theta = 0°$, rather than a directional JONSWAP spectrum. To proceed, we assume a monochromatic wave with $H_0=H_s$ and $T=T_p$ can be used as a proxy of the JONSWAP spectrum. The expectation is then that the calculated results should be qualitatively similar to the results in [14]; no exact quantitative agreements are expected in this initial research.

Among the many cases discussed in [14], we only consider one case: see their Fig. 3(a). For this case, the WEC-induced wave shadow function is given by their Fig. 3(d) in the form of breaking wave height H_b as a function of y. After filtering out the fluctuations and

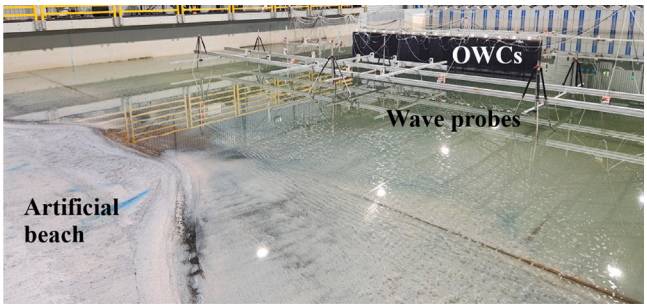

Fig. 7. 16 OWCs arranged to a "breakwater" configuration (no spacing between devices). Although the beach is initially straight, at the end of the experiment (after the impact of 54 000 incoming waves), a salient is formed in the photo, due to nearshore currents. Taken from [12]. See also Fig. 8(d) for the salient.

normalising, Fig. 6(a) of the present paper is obtained, which is used as the function $f(y)$ needed to calculate nearshore currents using Eq. (8). Note that we do not have access to the WEC array specifications and the array's hydrodynamic model, so that we cannot calculate wave field around the array. However, because $f(y)$ is given, nearshore currents can still be calculated. To compare with [14], we set $c = 0.00778$ in Eq. (8). A proxy quantity for nearshore currents, denoted by V, the *surf zone averaged* longshore current is defined, to represent the aggregated effects of nearshore currents:

$$V(y) = \frac{\int_{x_s}^{x_b} v\,\mathrm{d}x}{x_b - x_s}, \tag{16}$$

i.e. the cross-shore (x-direction) average of the depth-averaged Eulerian longshore velocity v (Eq. (15)). A positive (negative) V indicates flow towards the positive (negative) y-axis. The results, as well as the extracted data from Fig. 3(j) of [14], are shown in Fig. 6(b). Qualitative agreement is observed.

Overall, although simplifications are introduced, the method captures the key features of a case attempting to model a realistic scenario.

3.3. Comparing calculated currents with basin experiments

Results from an experiment conducted in [12] are now revisited. A 16-device OWC array arranged to a "wall" or a "breakwater" (*i.e.* no space between adjacent devices), placed at the end of the beach ($x = 8.79$ m, see Fig. 7) is studied. The array position in the coordinate system is shown in Fig. 8(a). The normalised wave shadow function $f(y)$ is measured at $x = 5.25$ m by wave probes (Fig. 8b) and it is assumed that its shape persists until the wave breaking point $x = x_b = 0.861$ m (the value of x_b is calculated in the Supplementary Material). Although such an assumption leads to error, it is required, as no measurement was carried out during the experiment for $x < 5.25$ m.

With the above-mentioned $f(y)$, nearshore currents are calculated, with the empirical coefficient c chosen to be 0.03 in Eq. (8). The results are shown in Fig. 8(c), using $T = 1.6$ s and $H_0 = 0.05$ m to represent the JONSWAP spectrum used in [12] which used $T_p = 1.6$ s and $H_s = 0.05$ m. The "V" shaped wave shadow in Fig. 8(b) leads to a pair of dominant nearshore circulation cells in panel (c). The calculated currents concur in terms of general direction with the dye experiment observations in panel (d) of Fig. 8.

Some additional comments are in order:

(1) arrows in Fig. 8(c) only indicate current directions but not magnitudes; the latter are shown by colour grading;
(2) in Fig. 8(c), outside of the surf zone ($x > x_b$), the current velocity quickly diminishes, evidenced by the blue colour which represents near-zero velocity;

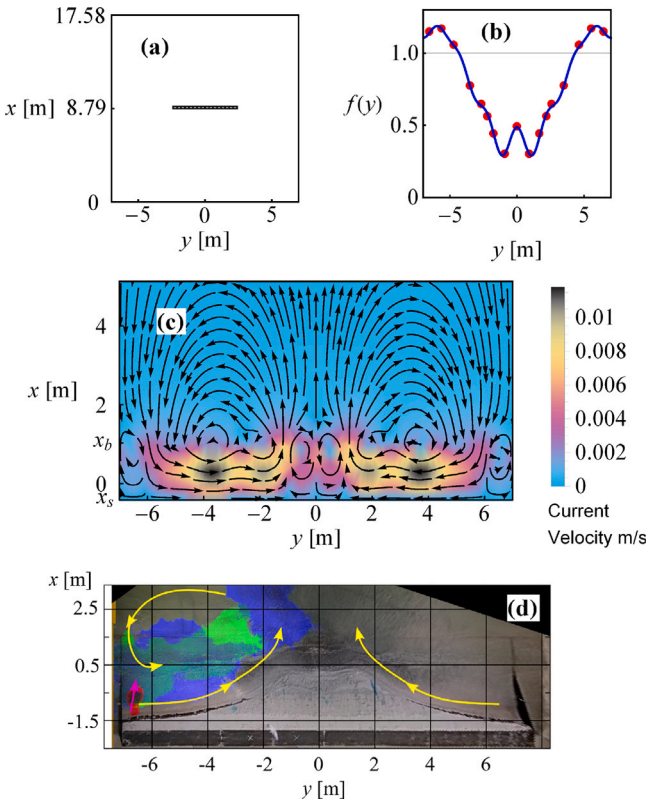

Fig. 8. Beach erosion due to a wall-shaped WEC array in [12] involving 16 OWCs. (a): top view of the OWC array layout, using black dots to indicate locations of WECs; (b) measured wave shadow function $f(y)$ at $x = 5.25$ m. Red dots: wave probe data; blue curve: Fourier series fit; (c) nearshore current calculated with $c = 0.03$. Arrows indicate current direction, while colour scales show current speed (m/s); (d) Using the same coordinate system as sub-plot (c) but using a different plot range for x, nearshore circulation patterns are inferred from the observed directions of dye transport (reproduced from [12]). Yellow arrows indicate the dominant current direction, while the magenta arrow denotes the initial spreading of the dye immediately after release. The image is an overlay of three time-separated frames extracted from a video, with the dye colourised differently at each timestamp to illustrate its temporal evolution. The arrows were determined qualitatively by visual inspection of the video and are intended as indicative only.

(3) the choice $c = 0.03$ for plotting Fig. 8(c) is arbitrary; it ensures that the resulting current velocities are of the correct order of magnitude. The true value of c will almost certainly be different, but since it only changes the magnitudes (*i.e.* not the directions) of the currents, it will not affect the topology in Fig. 8(c);
(4) a quantitative comparison between Fig. 8(c) and (d) is impossible, due to the assumptions made and due also to the fact that the beach used to generate Fig. 8(c) is perfectly 2D, while the beach in Fig. 8(d) is the already-modified beach (showing 3D features).

Overall, although [12] did not focus on quantifying currents, the dye experiment in [12] as shown in Fig. 8(d) does not contradict with the calculated results shown in Fig. 8(c). This encourages further experiments dedicated to nearshore currents for more quantitative comparisons.

4. Sediment transport, beach erosion, power, and array optimisation

Having obtained nearshore currents, their geomorphological consequence is examined. We calculate a quantity called *bulk longshore*

sediment transport rate, whose gradient can quantify beach erosion or accretion. We then find array that maximises beach accretion or instead, leads to a "smooth" shaped beach. The power-generation ability of these arrays is compared against a maximum-power array at the end of this section.

4.1. Sediment transport model: based on bulk longshore sediment transport rate

The following formula for the bulk longshore sediment transport rate, Q_{ls}, is proposed in [24]:

$$Q_{\mathrm{ls}} = \frac{\varepsilon}{(\rho_{\mathrm{s}} - \rho)(1-\varphi)g w_{\mathrm{s}}} FV \tag{17}$$

where ρ_{s} is the density of sediment (1500 kg/m^3 in [14], 1320 kg/m^3 in [12]), ρ is the water density (1000 kg/m^3), φ is the sediment porosity (0.4 in [14] and approximately 0.55 for [12]), w_{s} is the sediment fall velocity (0.03 m/s in [14], 0.016 m/s for [12] according to a formula given by [41]). The surf-zone averaged longshore velocity V is defined by Eq. (16). The wave energy flux (wave power) F is given by $F = Ec_{\mathrm{g}}$ where the wave energy density E for the incident monochromatic wave with wave height H is defined by

$$E = \frac{1}{8}\rho g H^2,$$

and the group velocity c_{g} is calculated by (using $\omega^2 = gk\tanh(kh)$):

$$c_{\mathrm{g}} = \frac{\mathrm{d}\omega}{\mathrm{d}k} = \frac{\omega}{2k}\left[1 + \frac{2kh}{\sinh(2kh)}\right], \tag{18}$$

where H, h, k are evaluated at the wave breaking location x_{b}. Finally, ε in Eq. (17) is a transport coefficient, which should be distinguished from the small parameter ϵ in Eq. (4).

4.2. Erosion metrics

The gradient of Q_{ls} along the beach is given by

$$\frac{\mathrm{d}Q_{\mathrm{ls}}}{\mathrm{d}y} \tag{19}$$

which is directly related to beach erosion or accretion: a positive $\mathrm{d}Q_{\mathrm{ls}}/\mathrm{d}y$ suggests an increase in sediment transport as y increases, which implies a sediment loss (deficit), leading to beach erosion. Conversely, a negative gradient signifies that the longshore transport decreases, which leads to beach accretion. Hence, if one plots $-\mathrm{d}Q_{\mathrm{ls}}/\mathrm{d}y$ (note the deliberately added negative sign) along a beach, and calculates the ratio of the negative area (erosion zones) to the positive area (accretion zones), a ratio greater than 1 suggests that the total accretion outweighs erosion, so the beach grows in volume. The absolute value of $\mathrm{d}Q_{\mathrm{ls}}/\mathrm{d}y$ for a given y determines how fast the sediment is being deposited or removed (rate of growth) at that y.

4.3. Comparing beach erosion with the example in Section 3.2

In [14], the precise value of ε in Eq. (17) is not given, but we estimate that $\varepsilon \approx 0.012$ and use it in this paper. The exact value of ε does not change the topology of the Q_{ls} curve in this paper, and it is the topology that we are most interested in.

For the case in Section 3.2, calculating Q_{ls} and $-\mathrm{d}Q_{\mathrm{ls}}/\mathrm{d}y$ using the formula listed in Section 4.1, the results are plotted in Fig. 9; the figure can be compared directly to Fig. 7(a) of [14]; qualitative agreements in trends are obtained, although quantitative comparisons are not attempted due to the model simplifications as well as the assumptions explained in Section 3.2.

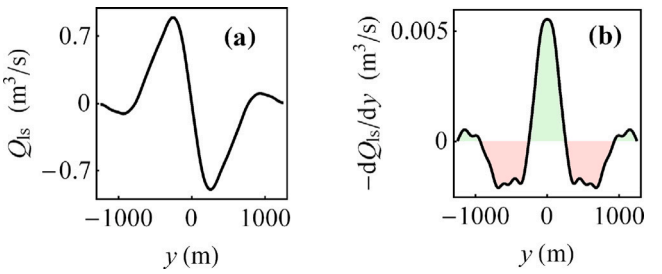

Fig. 9. Reproducing Fig. 7(a) of [14] by the method in this paper. Panel (a) shows longshore sediment transport rate Q_{ls} given by Eq. (17) with $\varepsilon = 0.012$; panel (b) shows $-\mathrm{d}Q_{\mathrm{ls}}/\mathrm{d}y$; green shadings refer to beach accretion while red shadings correspond to beach erosion. Combining the two panels gives Fig. 7(a) of [14].

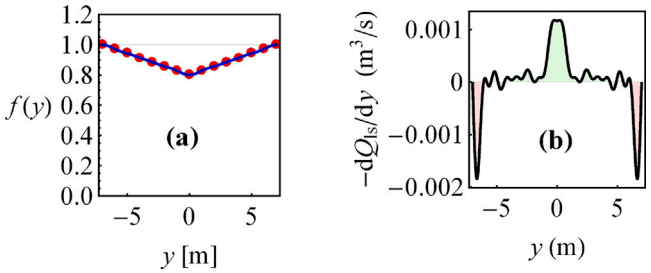

Fig. 10. Beach erosion due to the initial $f(y)$ introduced in Section 4.4.2. (a) the initial $f(y)$ curve; (b): $-\mathrm{d}Q_{\mathrm{ls}}/\mathrm{d}y$; green refers to beach accretion while red, erosion.

4.4. Design objective I: maximising net accretion

4.4.1. An area ratio

It was explained in Section 4.2 that the positive area of the $-\mathrm{d}Q_{\mathrm{ls}}/\mathrm{d}y$ curve corresponds to beach growth, while the negative area suggests beach erosion. Define the *ratio* of the positive area relative to the negative area as a growth factor, $\mathfrak{G}$:

$$\mathfrak{G} \equiv \frac{\text{positive area of the } (-\mathrm{d}Q_{\mathrm{ls}}/\mathrm{d}y) \text{ curve}}{\text{negative area of the } (-\mathrm{d}Q_{\mathrm{ls}}/\mathrm{d}y) \text{ curve}}. \tag{20}$$

It is understood that even when other parameters (*e.g.* the area under the $f(y)$ curve) are controlled, $\mathfrak{G}$ is still not the sole criterion in grading the performance of WEC arrays, because the uneven distribution of $\mathfrak{G}$ along the beach is also important. In this sense, $\mathfrak{G}$ is only one of the criteria; pursuing a large $\mathfrak{G}$ is primarily of academic interest; it is unlikely to become the final design criterion. In what follows, we first focus on finding a $f(y)$ curve that maximises $\mathfrak{G}$ without discussing which WEC array can create it. After this, we move on to consider WEC arrays.

4.4.2. Which $f(y)$ curve yields a large growth factor?

In this sub-section, $\mathfrak{G}$ for a multitude of $f(y)$ curves with the same area but different shapes are compared, with the aim of finding which $f(y)$ curve maximises $\mathfrak{G}$. The $f(y)$ curves are discussed without the context of WEC arrays.

To facilitate future experimental studies, the beach considered here will be the same as that in [12], *i.e.* Fig. 2, spanning over $y = (-7, 7)$ m. Offshore monochromatic wave height is $H_0 = 0.05$ m, with period $T = 1.6$ s.

The starting $f(y)$ is "V" shaped (the blue curve in Fig. 10a, inspired by the shape of $f(y)$ in Fig. 8b), with an area coefficient $c_{\mathrm{A}} = 0.9$. The area coefficient c_{A} is defined as:

$$c_{\mathrm{A}} \equiv \frac{\int_{-L}^{L} f(y)\mathrm{d}y}{2L} \tag{21}$$

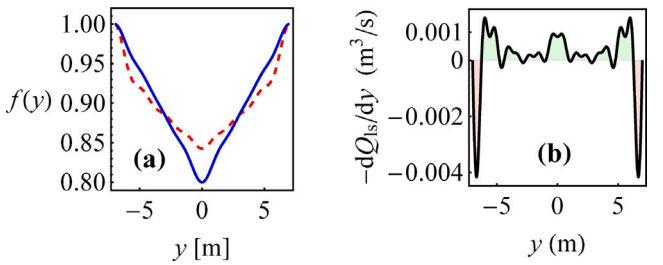

Fig. 11. (a) an optimised $f(y)$ (red dashed) compared with the initial $f(y)$ (blue). Note the plot range is from 0.80 to 1.00; (b): $-\mathrm{d}Q_{\mathrm{ls}}/\mathrm{d}y$ curve, for which $\mathfrak{G} = 1.342$.

where $2L$ is the length of the beach. The corresponding $-\mathrm{d}Q_{\mathrm{ls}}/\mathrm{d}y$ curve is given in Fig. 10(b), for which $\mathfrak{G} = 1.244$. Although this value is already decent, we seek to further increase $\mathfrak{G}$, *via* changing the shape of $f(y)$. The following constraints are imposed when searching for the optimum:

(1) regardless of the shape of $f(y)$, c_{A} must be within 0.9 ± 0.01;
(2) $f(y)$ must be symmetrical about $y = 0$;
(3) at the two ends of the beach, *i.e.* $y = -L = -7$ m and $y = L = 7$ m, it is required that $f(y) = 1$. This is an arbitrary but reasonable and convenient value;
(4) random perturbations are imposed to the 15 red-coloured data points on the initial $f(y)$ to obtain new data points that defines a new $f(y)$, with which $\mathfrak{G}$ is calculated. If $\mathfrak{G}$ is greater than 1.244, then the new $f(y)$ is used as the new basis for further optimisations. This is repeated until the maximum number of iterations is exhausted;

With the maximum number of iterations set to 300, the optimisation routine produces the $f(y)$ curve in Fig. 11(a) (dashed red curve); the time to carry out the optimisation is approximately 20 min on a Dell Inspiron laptop computer equipped with an Intel Core i7 8558U CPU (base frequency 1.80 GHz) with 7.90 GB RAM, on Windows 10 (64-bit) operating system. The new $f(y)$ curve deviates from the original $f(y)$ in that the "valley" at $y = 0$ is shallower, and the removed area is re-distributed to $y = \pm 6$. The resulting $\mathfrak{G}$ value calculated according to Fig. 11(b) is 1.342.

Note that strictly, the "optimum" $f(y)$ curve shown in Fig. 11(a) is not the true optimum, because (1) the optimisation routine only performs a limited number of iterations; (2) the optimisation scheme relies on random perturbations to create new $f(y)$. However, running the optimisation routine multiple times, most runs produce a similar-shaped $f(y)$ curve with a similar $\mathfrak{G}$ value, suggesting that the $f(y)$ curve found by such a method is one of the robust solutions.

4.4.3. WEC array producing maximum net accretion

Now consider a model WEC array suitable for the wave basin test shown in Fig. 1 for protecting the laboratory beach shown in Fig. 2. The key result will be a layout of WEC array generating a suitable $f(y)$ leading to a relatively large $\mathfrak{G}$ value. The optimisation procedure itself is simple and is described in Appendix B; here we focus on the resulting hydrodynamic and geomorphological effects.

The resulting array layout suggested for the basin is shown in Fig. 12(a), together with the transmission coefficient of incident waves around the array. Taking a slice of Fig. 12(a) at $x = 2.75$ m, one obtains the function $f(y)$ in Fig. 12(b). This function is similar to the dashed curve in Fig. 11(a), although in the current case, the two extremities of $f(y)$ are no longer forced to be equal to 1: $f(\pm 7) < 1$ in Fig. 12(b). Panel (c) shows Q_{ls} calculated with the aforementioned $f(y)$. The key quantity related to beach erosion, $-\mathrm{d}Q_{\mathrm{ls}}/\mathrm{d}y$, is given by panel (d), which is similar to Fig. 11(b). Such similarity is striking,

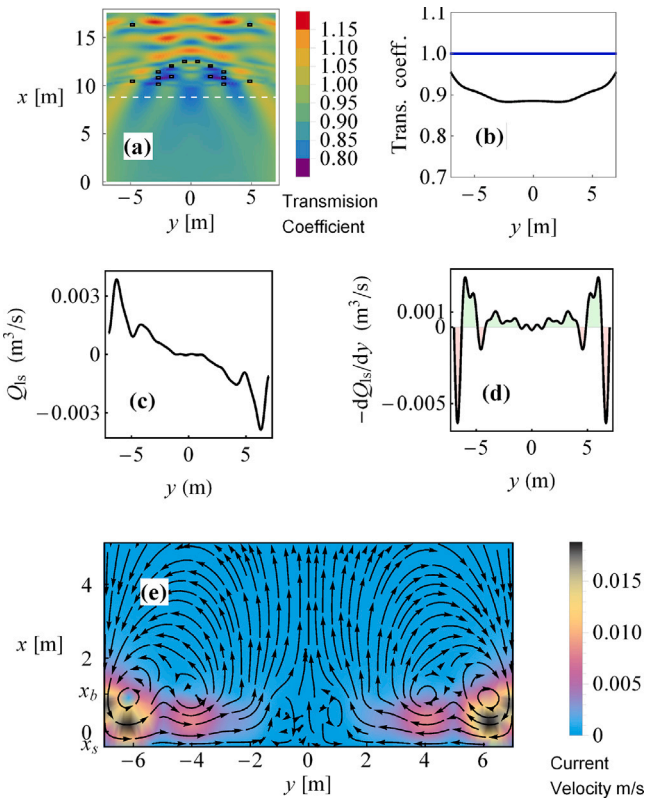

Fig. 12. An array leading to large growth factor $\mathfrak{G}$. (a) wave field: plot of array layout and wave transmission coefficient of incident waves. Devices are represented by drawn-to-scale (0.2×0.3 m) rectangles. The dashed white line marks the end of the beach ($x = 8.79$ m). The transmission coefficient plot is generated using the method in [17], assuming a flat sea bottom (*i.e.* neglecting the beach slope in this paper); (b) wave shadow: the function $f(y)$, which is a cross-section of plot (a) at $x = 2.79$ m (*i.e.* 6 m away from the end of the beach); (c): the Q_{ls} curve. (d): $-\mathrm{d}Q_{\mathrm{ls}}/\mathrm{d}y$ curve, for which $\mathfrak{G} = 1.323$. (e) nearshore currents.

because although the present array optimisation does not start with a "V" shaped initial $f(y)$ as in Fig. 11(a), the final result is similar. The nearshore currents are shown in Fig. 12(e).

An obvious feature of Fig. 12(d,e) is that local erosion and accretion "hotspots" are observed near $y = \pm 6$ m, similar to Fig. 11(b). Consequently, a high $\mathfrak{G}$ does not necessarily reduce the risk of localised extreme erosion (*e.g.* deep scour rip channels amid general accretion). Although in reality, these hotspots may not translate directly to intense localised beach erosion/accretion (*e.g.* due to nonlinear effects, limitations in modelling), in the next section, a new optimisation goal is proposed to avoid these hotspots to promote more predictable shoreline behaviour.

4.5. Design objective II: minimising erosion hotspots

In the previous section, we showed that while maximising $\mathfrak{G}$ improves beach accretion, it may cause localised erosion hotspots. To address this, we redefine the optimisation objective by minimising the following quantity:

$$S \equiv \int_{-L}^{L} \left[\left(\frac{\mathrm{d}Q}{\mathrm{d}y} \right)^2 + \left(\frac{\mathrm{d}^2 Q}{\mathrm{d}y^2} \right)^2 \right] \mathrm{d}y, \tag{22}$$

where, minimising the first derivative term avoids sharp gradients (*i.e.* sudden erosion/accretion jumps); minimising the second derivative term reduces curvature of the Q_{ls} curve, increasing smoothness.

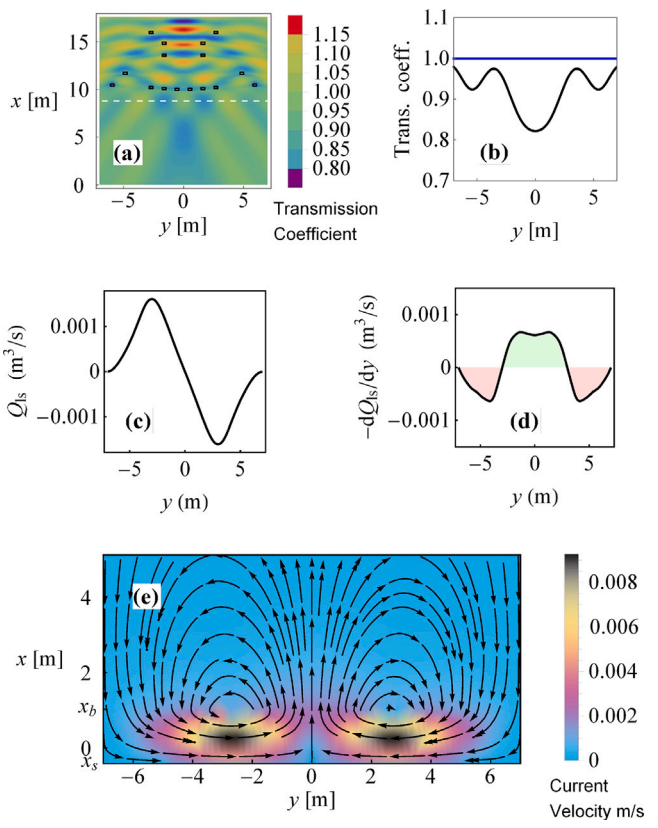

Fig. 13. An array leading to "smooth" erosion curve (minimising $\mathcal{S}$). (a) wave field: plot of array layout (rectangles are OWCs viewed from top) and wave transmission around the array; (b) wave shadow: the function $f(y)$, given by a cross-section of plot (a) at $x = 2.79$ m; (c): Q_{ls}. (d): $-dQ_{ls}/dy$ curve, for which $\mathfrak{G} = 1.005$ and $S = 5.97 \times 10^{-6}$. (e) nearshore currents.

Minimising the sum of the two is expected to help avoid erosion and accretion hotspots in the previous section.

Using only step 1 of optimisation in Appendix B, the array layout in Fig. 13 is obtained. Despite the array's irregular appearance it produces much smoother dQ_{ls} and $-dQ_{ls}/dy$ curves, panels (c) and (d). The latter shows no erosion and accretion "hotspots"; instead, only one centralised accretion region that transits smoothly to neighbouring erosion regions is observed. The nearshore currents in panel (e) has only one pair of cells.

4.6. Power-generation considerations

So far, the present paper did not consider power generated by the OWC array in its optimisation studies. Power extraction is of central importance to traditional WEC arrays. However, for dual-purpose array design, its importance can be reduced compared with the arrays' coastal impacts. As [12] already implied, arrays with similar power outputs can give rise to qualitatively different beach responses. In the present paper, this is also true. Specifically, for the 16-same-device arrays considered, for a particular monochromatic wave frequency ω, the absorbed power of device i is given by:

$$P_i(\omega) = \frac{1}{2} K_{\mathrm{PTO}}\, \omega^2\, |\Xi_i(\omega)|^2. \tag{23}$$

where K_{PTO} is PTO damping and Ξ is the response amplitude in an OWC device. Hence the total array power scales as

$$P_{\mathrm{array}} \propto \sum_{i=1}^{16} |\Xi_i|^2. \tag{24}$$

Accordingly, $\sum_{i=1}^{16} |\Xi_i|^2$ can be employed as a relative performance indicator for comparing array layouts. Using the optimisation procedure in Appendix B but changing the objective to maximising $\sum_{i=1}^{16} |\Xi_i|^2$, one obtains 0.05174 as the optimal value. Comparably, for the array layout in Fig. 12, the corresponding value is 0.04892; while for the layout in Fig. 13, the value is 0.05002. Both of them are not far from the best value (only 5.45% and 3.33% lower, respectively). In view of that, as an initial study we refrain from adding the (well-known) power analysis into the optimisation framework, to ensure that the focus is on explaining the (relatively less well-studied) coastal protection aspects thoroughly. Finally, we note in passing that since the power removed by a PTO can be controlled, it is possible to operate the array in two modes: power generation and coastal protection.

5. Conclusion

From a methodological perspective, the present semi-analytical approach enables a computationally inexpensive link between an arbitrary wave shadow function and beach responses. Previous semi-analytical treatment of currents [23] was restricted to idealised sinusoidal perturbations in wave height (unrealistic for WEC arrays) and it did not consider sediment transport, while numerical models [*e.g.* 14] capable of handling WEC-generated wave fields remain costly for large-scale optimisation studies. By generalising the classic formulation of [23] to arbitrary wave shadow shapes and coupling it to a sediment transport model and a WEC-wave interaction model, the present method bridges the above gap and allows hundreds of array layouts to be assessed within $O(10)$ minutes on an entry level laptop computer.

Physically, the results show that the shape (spatial distribution) of the wave shadow along the shoreline plays a more important role than its magnitude, concurring with [12]. Arrays that produce similar overall reductions in wave energy can generate qualitatively different nearshore circulation patterns. In particular, sharp gradients in the wave shadow tend to create erosion hotspots, whereas smoother variations correspond to gentler shoreline response. This implies that maximising wave attenuation [*e.g.* 17] is insufficient as a coastal protection strategy.

From an engineering point of view, the optimisation studies indicate that the rip currents behind WEC arrays [42] can be controlled. This study also demonstrated that prioritising coastal protection does not necessarily imply a significant sacrifice in energy generation performance. Arrays optimised for sediment transport characteristics can achieve power absorption levels close to those of arrays optimised purely for energy extraction. Hence (for the OWCs and wave conditions considered here) coastal protection and power generation can be co-optimised. This finding supports the viability of dual-purpose WEC arrays as adaptive infrastructure, capable of responding to evolving shoreline management needs without undermining their role as renewable energy sources.

As an initial study, the model is subject to several limitations. It relies on simplifications such as monochromatic, normally incident waves, linearised governing equations for currents (lacking a proper model for viscous effects), and empirical parameters that may vary across sites. It also assumes a simple planar beach, flat offshore bathymetry, and neglects wave–current interactions in the surf zone. The WEC array model assumes the wave shadow function $f(x, y)$ is unaffected by shoaling. While qualitative agreement with laboratory and numerical experiments was found, dedicated experimental validation is required.

CRediT authorship contribution statement

Lidong Cui: Writing – original draft, Visualization, Methodology, Investigation, Formal analysis, Data curation, Conceptualization. **Nataliia Y. Sergiienko:** Validation, Software, Resources, Formal analysis,

Data curation. **Nadav Cohen:** Writing – review & editing, Visualization, Validation, Resources, Investigation, Data curation. **Justin S. Leontini:** Writing – review & editing, Validation, Software, Project administration, Methodology, Investigation, Funding acquisition. **Benjamin S. Cazzolato:** Writing – review & editing, Validation, Supervision, Resources, Project administration, Funding acquisition. **Francois Flocard:** Supervision, Resources, Project administration, Funding acquisition, Data curation, Conceptualization. **Richard Manasseh:** Writing – review & editing, Supervision, Resources, Project administration, Methodology, Investigation, Funding acquisition, Formal analysis, Conceptualization.

Declaration of competing interest

The authors declare that they have no known competing financial interests or personal relationships that could have appeared to influence the work reported in this paper.

Acknowledgements

This research was funded by the Australian Government through the Australian Research Council (project number ARC LP180101109). N. S. received an Australian Research Council Early Career Industry Fellowship (IE230100545) funded by the Australian Government. The authors thank three anonymous referees and the Executive Editor for constructive advice.

Appendix A. Comparing with a classic example

In [23], whose method is used as a foundation of the present study, the beach slope $\widetilde{m} = 1/12$ and the offshore water depth is $h_0 = 0.75$ m. Offshore wave height is $H_0 = 0.0645$ m with period $T = 1.14$ s. The author considered a canonical form of $f(y)$ consisting of only one cosine function (*i.e.* $N = 1$ in Eq. (6)) generated by *e.g.* edge waves [43]. It reads

$$f(y) = 1 + \epsilon \cos(\lambda y), \tag{A.1}$$

where $\epsilon \ll 1$, suggesting that the y-dependent term is relatively small. The exact value of ϵ does not qualitatively change the results; here it is set to 0.2. Moreover, λ is a nondimensionalised wavenumber, set to be a proportion of x_b (see p. 5745 of [23]):

$$\lambda = \frac{2\pi}{5x_\mathrm{b}}. \tag{A.2}$$

Note that Eq. (A.2) does not apply to any other case in this paper.

The bottom friction coefficient c in Eq. (8) is assumed to be (see p. 5745 of [23]):

$$c = -\frac{1}{1.6}\frac{B_1\widetilde{m}^2(1-K)^2}{\lambda^4} \tag{A.3}$$

where B_1 is defined by Eq. (7). Similar to Eq. (A.2), Eq. (A.3) does not apply to any other case of this paper.

To implement the method in this paper, discretising the function Eq. (A.1) to obtain 15 data points (red dots in Fig. A.14a), and use an 8-term Fourier series (*i.e.* $N = 7$ in Eq. (5)) to describe it (blue curve in Fig. A.14a). The results are shown in Fig. A.14(b, c). Fig. A.14(c) is explained first. It plots the streamfunction ψ given by combining Eqs. (10) and (12) to cover both the surf zone ($x < x_\mathrm{b}$) and the shoaling zone ($x > x_\mathrm{b}$). Note that the λy range is limited to $(0, \pi)$. As a result, Fig. A.14(c) shows only one circulation cell in a pair; the other cell that resides in $\lambda y \in (\pi, 2\pi)$ is a mirror image of the shown cell. Between these two cells, at $\lambda y = \pi$, a rip current flowing from the beach to the ocean exists. Fig. A.14(b) is a cross-section of the streamfunction in Fig. A.14(c) at $\lambda y = \pi/2$, showing that the current activity reaches maximum near the wave breaking point x_b. These plots are drawn in the same style as Fig. 6 of [23] to facilitate comparison: the streamlines

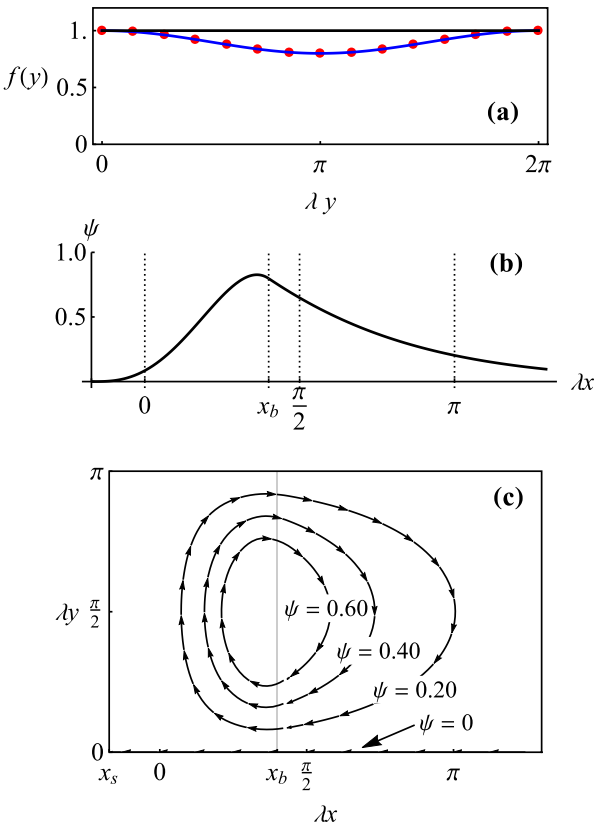

Fig. A.14. Reproducing Fig. 6 of [23] by the method in this paper. (a) the wave shadow function $f(y)$ (*cf.* Eq. (6)). Red dots are data points while the blue curve is Fourier series fit; (b) cut-away of panel (c) at $\lambda y = \pi/2$; (c): stream function ψ.

in Fig. A.14(c) show direction only; their magnitudes rely on additional labels on curves. These plots replicate the results of [23], providing a validation of the algorithm of the current paper.

Appendix B. Additional details for Section 4.4.3

The constraints of optimisation are:

(1) same as the case in Section 3.3, the array will consist of 16 OWC-type devices with the same specifications (detailed in the Supplementary Material);
(2) the array is placed offshore where the bottom is flat (see *e.g.* Fig. 1a). The array's location should not be too far from the beach, for experimental viability and for beach protection effectiveness. The first row of the array must be located at $x > 8.79$ m, while the last row should be placed within $x < 2 \times 8.79 = 17.58$ m. The first condition ensures that no part of the array is on the beach; the second condition ensures the array size does not exceed the size of the experimental section of a wave basin;
(3) the spanwise extent of the array is restricted to $y \in (-5.94, 5.94)$ m to avoid device being placed close to the edge of the wave basin;
(4) the minimum centre-to-centre distance between two devices must be above zero, to avoid obtaining the same "wall-like" array in Section 3.3;
(5) it is assumed that the wave shadow function $f(x, y)$ downwave of the array is unaffected by the presence of the beach, *i.e.* $f(x, y)$ at a beach location x is the same as if the water depth at x is the offshore water depth, 0.586 m. Such an assumption is partially justified in view of Eq. (SM19) in the Supplementary

Material where the height of the waves on the beach is linearly proportional to the offshore wave height H_0.

(6) the $f(y)$ used in Eq. (5) is $f(x, y)$ evaluated at $x = 2.75$ m.

(7) other aforementioned assumptions remain, *e.g.* neglecting wave–current interactions, *etc.*

A two-step optimisation scheme is implemented:

S1 *obtaining a "good" array by a random search.* Each device's y-coordinate is randomly chosen from a list of six values given by $0.54 + 1.08n, n = 0, 1, 2...5$, *i.e.* $\{0.54, 1.62, \ldots, 5.94\}$. This is to ensure that the y-distance between each column of the array is at least three times the characteristic dimension of the OWC to allow access to devices by creating "navigable channels" aligned with the x-direction. This is practical, because the wave is assumed to incident along the x-direction, and it is generally safer for a maintenance vessel to sail along the x-direction ("head seas") instead of the y-direction ("beam seas"). The x-coordinate of a device is a random number between $(8.89, 17.48)$. The lower bound 8.89 m is 0.1 m more than 8.79 m, and the upper bound is 0.1 m less than 17.58 m, considering that the device's half-thickness is $0.2/2 = 0.1$ m. Note that unlike the y-coordinate which can only be chosen from six values, a device's x-coordinate choices are infinite. During a typical random search, 300 different arrays are considered. The array with the largest $\mathfrak{G}$ is chosen.

S2 *perturbing the "good" array to find a "better" array.* The coordinates of the "good" array are perturbed; each coordinate is changed in small steps (*e.g.* 0.1 m) to explore whether these changes improve $\mathfrak{G}$ of the array. If no improvement is found, the code attempts a larger random perturbation to escape the local maxima. The code keeps track of the best configuration found, and produces updates whenever an improvement in $\mathfrak{G}$ occurs. This is a simple trial-and-error strategy, using only the values of functions as guide, without needing derivatives or gradients of functions.

Appendix C. Supplementary data

Supplementary material related to this article can be found online at https://doi.org/10.1016/j.renene.2026.125497.

References

[1] M. Decastro, G. Lavidas, B. Arguilé-Pérez, P. Carracedo, N. DeCastro, X. Costoya, M. Gómez-Gesteira, Evaluating the economic viability of near-future wave energy development along the Galician coast using LCoE analysis for multiple wave energy devices, J. Clean. Prod. 463 (2024) 142740.

[2] IRENA, Renewable Power Generation Costs in 2024, International Renewable Energy Agency, Abu Dhabi, 2024.

[3] R. Manasseh, K. McInnes, M. Hemer, Pioneering developments of marine renewable energy in Australia, Int. J. Ocean. Clim. Syst. 8 (1) (2017) 50–67.

[4] D. Clemente, P. Rosa-Santos, F. Taveira-Pinto, On the potential synergies and applications of wave energy converters: A review, Renew. Sustain. Energy Rev. (ISSN: 1364-0321) 135 (2021) 110162.

[5] H. Wolgamot, W. Ebeling, J. Orszaghova, A. Kurniawan, Ocean Wave Energy in Australia, Blue Economy Cooperative Research Centre, 2024.

[6] J. Liu, A. Meucci, Q. Liu, A.V. Babanin, D. Ierodiaconou, X. Xu, I.R. Young, A high-resolution wave energy assessment of South-East Australia based on a 40-year hindcast, Renew. Energy 215 (2023) 118943.

[7] R. Ranasinghe, I.L. Turner, Shoreline response to submerged structures: a review, Coast. Eng. 53 (1) (2006) 65–79.

[8] M.R. Gourlay, Wave set-up and wave generated currents in the lee of a breakwater or headland, in: Coastal Engineering 1974, 1974, pp. 1976–1995.

[9] A.-R. Westcott, L.G. Bennetts, N.Y. Sergiienko, B.S. Cazzolato, Broadband near-perfect capture of water wave energy by an array of heaving buoy wave energy converters, J. Fluid Mech. 998 (2024) A5.

[10] L. Cui, N. Spinks, N.Y. Sergiienko, D. Tothova, J.S. Leontini, B.S. Cazzolato, R. Manasseh, Helmholtz-type resonator with increased tunability and reduced viscous loss with application to wave energy converters, Ocean Eng. 333 (2025) 121432.

[11] J. Falnes, J. Hals, Heaving buoys, point absorbers and arrays, Philos. Trans. R. Soc. A: Math. Phys. Eng. Sci. 370 (1959) (2012) 246–277.

[12] N. Cohen, Wave Energy Converter Array Impacts on Nearshore Processes and Shoreline Realignment (Ph.D. thesis), UNSW, 2025.

[13] L. Cui, J.S. Leontini, R. Manasseh, Optimising layout of wave energy converter arrays with respect to wave amplitude gradients associated with beach erosion, in: Australasian Fluid Mechanics Conference, AFMC, 2024.

[14] D.P. Rijnsdorp, J.E. Hansen, R.J. Lowe, Understanding coastal impacts by nearshore wave farms using a phase-resolving wave model, Renew. Energy 150 (2020) 637–648.

[15] J. Abanades, D. Greaves, G. Iglesias, Wave farm impact on the beach profile: A case study, Coast. Eng. 86 (2014) 36–44.

[16] N.Y. Sergiienko, P.A. Cannard, L. Cui, J.S. Leontini, R. Manasseh, B. Cazzolato, Impact of wave energy converters on infragravity waves: An experimental investigation, Ocean Eng. 309 (2024) 118345.

[17] L. Cui, N.Y. Sergiienko, J.S. Leontini, N. Cohen, L.G. Bennetts, B. Cazzolato, I.L. Turner, F. Flocard, A.-R. Westcott, F. Cheng, et al., Protecting coastlines by offshore wave farms: on optimising array configurations using a corrected far-field approximation, Renew. Energy 224 (2024) 120109.

[18] R.J. McCarroll, R.W. Brander, J.H. MacMahan, I.L. Turner, A.J. Reniers, J.A. Brown, A. Bradstreet, S. Sherker, Evaluation of swimmer-based rip current escape strategies, Nat. Hazards 71 (3) (2014) 1821–1846.

[19] R.M. Hassan, A.S. Elstohey, Effects of detached breakwaters on drowning due to rip and circulation currents, Int. J. Adv. Technol. Eng. Explor. 10 (99) (2023) 153.

[20] B. Cooper, J. Ledger, S. Daw, J. Lawes, Coastal Safety Brief: Rip Currents, Surf Life Saving Australia, Sydney, 2021.

[21] A.L. Shanks, S.G. Morgan, J. MacMahan, A.J. Reniers, M. Jarvis, J. Brown, A. Fujimura, L. Ziccarelli, C. Griesemer, Persistent differences in horizontal gradients in phytoplankton concentration maintained by surf zone hydrodynamics, Estuaries Coasts 41 (1) (2018) 158–176.

[22] C. Itosu, M. Miki, Wave-induced circulation in abalone fishing ground: generating mechanism and labratory investigation (in Japanese), Fish. Eng. 22 (1) (1985) 47–54.

[23] A.J. Bowen, Rip currents: 1. Theoretical investigations, J. Geophys. Res. 74 (23) (1969) 5467–5478.

[24] A. Bayram, M. Larson, H. Hanson, A new formula for the total longshore sediment transport rate, Coast. Eng. 54 (9) (2007) 700–710.

[25] I.L. Turner, D. Whyte, B. Ruessink, R. Ranasinghe, Observations of rip spacing, persistence and mobility at a long, straight coastline, Mar. Geol. 236 (3–4) (2007) 209–221.

[26] N. Kumar, G. Voulgaris, J.C. Warner, Implementation and modification of a three-dimensional radiation stress formulation for surf zone and rip-current applications, Coast. Eng. 58 (12) (2011) 1097–1117.

[27] J. Yu, On the instability leading to rip currents due to wave–current interaction, J. Fluid Mech. 549 (2006) 403–428.

[28] M. Hino, Theory on formation of rip-current and cuspidal coast, Coast. Eng. Jpn. 17 (1) (1974) 23–37.

[29] G. Coco, A.B. Murray, Patterns in the sand: From forcing templates to self-organization, Geomorphology 91 (3–4) (2007) 271–290.

[30] M.S. Longuet-Higgins, R. Stewart, Radiation stress and mass transport in gravity waves, with application to 'surf beats', J. Fluid Mech. 13 (4) (1962) 481–504.

[31] B. Castelle, T. Scott, R. Brander, R. McCarroll, Rip current types, circulation and hazard, Earth-Sci. Rev. 163 (2016) 1–21.

[32] R.A. Holman, A. Sallenger Jr., Setup and swash on a natural beach, J. Geophys. Res.: Ocean. 90 (C1) (1985) 945–953.

[33] M.S. Longuet-Higgins, Longshore currents generated by obliquely incident sea waves: 1, J. Geophys. Res. 75 (33) (1970) 6778–6789.

[34] R.A. Dalrymple, C.J. Lozano, Wave-current interaction models for rip currents, J. Geophys. Res.: Ocean. 83 (C12) (1978) 6063–6071.

[35] E.K. Noda, Wave-induced nearshore circulation, J. Geophys. Res. 79 (27) (1974) 4097–4106.

[36] R.A. Dalrymple, A mechanism for rip current generation on an open coast, J. Geophys. Res. 80 (24) (1975) 3485–3487.

[37] A. Valipour, A. Bidokhti, An analytical model for the prediction of rip spacing in intermediate beaches, J. Earth Syst. Sci. 127 (8) (2018) 108.

[38] B. Castelle, G. Masselink, Morphodynamics of wave-dominated beaches, Camb. Prism.: Coast. Future 1 (2023) e1.

[39] C.C. Mei, M.A. Stiassnie, D.K.-P. Yue, Theory and Applications of Ocean Surface Waves: Part 2: Nonlinear Aspects, World Scientific, 2005.

[40] M.E. McCormick, Ocean Engineering Mechanics: with Applications, Cambridge University Press, 2009.

[41] R. Ferguson, M. Church, A simple universal equation for grain settling velocity, J. Sediment. Res. 74 (6) (2004) 933–937.

[42] X. Cao, J. Shi, J. Zheng, C. Zhang, J. Pan, Offshore wave energy converter array poses threat to coasts causing significant rip currents, Physics of Fluids 37 (8) (2025).

[43] R.T. Guza, R.E. Davis, Excitation of edge waves by waves incident on a beach, J. Geophys. Res. 79 (9) (1974) 1285–1291.